Materials Characterization 203 (2023) 113048

Contents lists available at ScienceDirect

Materials Characterization

journal homepage: www.elsevier.com/locate/matchar

Microstructural, chemical, and mechanical characterization of extruded Al-Cu-Li rods

Paula Rodríguez-González [a,*], Miguel Ángel Monge [b], Elena Gordo [a], Elisa María Ruiz-Navas [b]

[a] Departamento de Ciencia e Ingeniería de Materiales e Ingeniería Química, IAAB, Universidad Carlos lll de Madrid, Avda. Universidad 30, 28911 Leganés, Spain
[b] Departamento de Física, Universidad Carlos lll de Madrid, Avda. Universidad 30, 28911 Leganés, Spain

ARTICLE INFO

Keywords:
Aluminium–lithium alloys
Extrusion
Powder metallurgy
Microstructure
Chemical properties
Mechanical properties

ABSTRACT

This work investigates the influence of the alloying elements in rods of the alloys Al-Cu-Li produced by novel powder metallurgy routes. In the first route, the powders were mixed and uniaxial cold-pressed, followed by hot extrusion to produce 5 mm diameter rods. The second route introduced an intermediate step of heat treatment that was carried out at 525 °C for 1 h in a pure N2 atmosphere before the extrusion. This was done to evaluate the importance of homogenization of the alloying elements during the heat treatment, as well as the tendency to form new phases in the extruded rods. The obtained rods were characterized by SEM, EBSD, Vickers microhardness, chemical composition (ICP-OES), and tensile tests. The results obtained showed that the alloy 1 (AA2060) presents a more homogeneous microstructure than alloy 2 (AA2196), and it is observed the benefit of Mg addition, which improves the microstructure after HT. The EBSD analysis showed a typical preferential orientation of a duplex fiber texture. The ICP-OES analysis reports losses of Li and Mg for both alloys. Regarding to the measurement of hardness, the results were very different depending on the alloy and the HT prior to the extrusion process.

1. Introduction

The most widely used aluminium alloys in the aerospace industry are the Al-Cu alloys (2xxx series) and the Al-Zn alloys (7xxx series) due to their high strength-to-weight ratio. Specifically, aluminium-lithium alloys are interesting for this industry because the addition of lithium significantly reduces the density of the alloy while increasing the strength much more than with any other alloying element; Each increment of 1 wt% lithium alloyed with aluminium decreases the density by 3% and increases the elastic modulus (E) by about 6% [1,2]. Aluminium-lithium alloys (Al-Li) are characterized by their high corrosion resistance and specific modulus, which makes it possible to save weight in the aircraft, thus reducing CO_2 emissions. In addition, they have excellent fatigue and cryogenic strength and superior resistance against fatigue crack growth.

Third-generation aluminium-lithium (Al-Li) alloys [3] are of great interest to the aerospace industry due to their advantages, which include excellent corrosion resistance, greater fatigue resistance, high strength, good hardness, and significantly lower weight [4]. In addition, Al-Cu-Li alloys offer a cost advantage over CFRPs (Carbon Fiber Reinforced Polymers). For this reason, there has been increased interest in these alloys for new aircraft designs [5].

Regarding the third-generation alloys, Al_3Li (δ') is the strengthening phase in binary Al-Li alloys. However, the third generation also contains copper, and adding Cu to Al-Li alloys is more effective for strengthening. For Al-Cu-Li systems, the most important phases are T1 (Al_2CuLi), T2 (Al_6CuLi_3), and TB ($Al_{15}Cu_8Li_3$). C. Giummarra et al. [6] concluded that the ternary T1 (Al_2CuLi) phase is the primary strengthening phase, and the binary phases, such as δ'(Al_3Li) and θ'(Al_2Cu), contribute less to strengthening.

Some studies report limits in the ranges of lithium content that promote these phases [7]. The low Li contents (<0.6%) promote semi-coherent θ' and incoherent θ (Al_2Cu) phases [8], while the medium Li content (<1.4–1.5%) promotes semi-coherent T1 (Al_2CuLi) phase. Finally, the higher Li content (>1.4–1.5%) promotes coherent δ'(Al_3Li) precipitates. However, the conclusions of many studies relating to the Li: Cu ratio for these alloys seem to be more accurate. They establish that the precipitation sequence found for Al-Cu-Li alloys depends on the Li: Cu ratio, as shown by Hirano and Decreus et al. [9] and Prasad et al. [5]. In high lithium and low copper alloys (> 2 wt% lithium, <2 wt% copper)

* Corresponding author.
E-mail addresses: paularod@ing.uc3m.es (P. Rodríguez-González), mmonge@fis.uc3m.es (M.Á. Monge), egordo@ing.uc3m.es (E. Gordo), emruiz@ing.uc3m.es (E.M. Ruiz-Navas).

https://doi.org/10.1016/j.matchar.2023.113048
Received 15 March 2023; Received in revised form 21 May 2023; Accepted 27 May 2023
Available online 7 June 2023

precipitation of the T1 (Al_2CuLi) phases occurs and promotes δ′(Al_3Li) formation, which can be observed by TEM techniques. The sequence of precipitates Guinier Preston (GP) zones → θ″ → θ' → stable θ is favored for higher copper and lower lithium.

The rest of alloying elements also greatly influence the strengthening of the Al matrix. The Zn promotes the formation of the Al_3Zn phase. The formation of T1 is promoted by small additions of Mg and Ag. Mg reduces the solubility of Li in Al [7], and promotes the formation of phases such as GPB zones, the S′ (orthorhombic phase coherent, $Al_{10}Cu_3Mg_3$) and S (equilibrium phase, Al_2CuMg) phases [8], substituting Li for Mg in the T1 phase [10].

There are several third-generation alloys that are of great interest in the industry. Firstly, AA2060 is one of the most recent, launched in 2011 by Alcao Inc. [11], and which exhibits excellent corrosion resistance, high thermal stability and strength, along with good toughness [5,12,13]. Nowadays, the use of 2060-T8 alloy for fuselage skin and lower wing structures, replacing 2524-T3 and 2024-T351, can save 7% and 14% weight, respectively [12]. The good weldability properties of 2060 alloy have been explored in other research studies [5,14].

Secondly, some alloys, such as 2099, 2195 and 2198, have a long history in aerospace applications. AA2199 and AA2198 are used for sheet products in commercial aircraft. AA2099 and AA2199 were developed for space and aircraft applications due to their attractive properties [15]. AA2195 has been proposed for the Space Shuttle Super Lightweight External Tank [13]. Airbus chose AA2198 alloy for the fuselage skin sheet material of the A350 [16]. At the same time, AA2196 is in particular very promising since NASA uses it in extrusions for commercial aircraft [14], and it is also part of the Airbus A380 plane [5].

Aluminium is mainly processed by extrusion in which aluminium billets are heated and pushed through a shaped die opening. The extrusion process from billets of powders is known as a powder metallurgy (PM) route. PM routes are widely used in lightweight metals (Al, Ti, Mg). The automotive and aerospace sectors have driven these routes. Particularly the PM of Al is expected to experience significant growth in the next decade, the most crucial advantage is the elimination of melting material due to the use of diffusion processes that allow working with elements in the solid state and at low temperatures, thus avoiding material losses by evaporation from fusion techniques. This point is crucial not only in terms of the final cost and durability of the equipment but, in the case of Al, the fact that they eliminate all the harmful phenomena involved in aluminium fusion, such as cracking.

In previous research [17], the extrusion process was optimized to obtain fully dense rods. As the process is carried out at a low temperature without melting the material, the most suitable extrusion temperature was optimized for 2060 and 2196 alloys. The rods of 2060 and 2196 alloys were extruded with and without heat treatment before the extrusion process. The processing of both alloys was successfully processed by PM routes.

In this work, the effects of homogenization and the influence of composition and the processing for both alloys on the microstructure and properties of the materials such as mechanical properties, were studied. The new route proposed for processing opens up a wide range of possibilities for the design of chemical composition. The use of the powder makes it possible to tailor the chemical compositions according to the desired properties and to adapt to future requirements without melting the base material.

2. Experimental

The nominal compositions of the produced alloys are shown in Table 1. The alloys were fabricated starting from elemental powders of Al, Cu, Mn, and Zn, while Mg and Li were added as master alloys with compositions 92.1wt%Al/ 7.9wt%Mg and 80 wt% Al/ 20 wt%Li. There are two alloys selected. The main difference between them is the Li and Cu content and that they have a chemical composition based on the 2060 and 2196 aluminium alloys (Table 1). The main characteristics of the powders used are also summarised in Table 1.

Table 1
Chemical composition of alloys (wt%) of alloys and characteristics of the powders.

	Cu	Li	Mn	Mg	Zn	Al
Alloy 1: 2060	4.00	0.75	0.30	0.85	0.40	Bal.
Alloy 2: 2196	3.00	1.75	0.35	0.50	0.35	Bal.

Characteristics of the powders

Powder	Provider	Particle size (μm)	Purity (%)
Aluminium	AEE, upper Saddle River, NJ USA	45	99.9
Aluminium/magnesium ($Al_{92.1\ wt\%}/Mg_{7.9\ wt\%}$) atomized	Goodfellow ltd., Huntingdon, UK	<30	99.0
Zinc	Goodfellow ltd., Huntingdon, UK	Range 1–10	99.0
Copper	Sigma Aldrich, Madrid, Spain	Range 14–25	98.0
Manganese	Sigma Aldrich, Madrid, Spain	<45	99.9
Aluminium/Lithium ($Al_{80\ wt\%}/Li_{20\ wt\%}$)	Sigma Aldrich, Madrid, Spain	<100	–

Powders were blended in a Turbula Mixer and compacted by uniaxial cold pressing at 600 MPa to obtain cylinders of 25 mm diameter with a relative green density of 99%. Zinc stearate was used as a wall-die lubricant. Extrusion of the powder compacts was performed in a conical die with an angle of 45°, at 525 °C using an extrusion ratio of 25:1, selected to ensure the complete densification of produced material, and were air cooled after the extrusion process. A mixture of graphite and gear oil was used as a lubricant. The rods obtained were 5 mm in diameter and 200 mm in length.

The first route consists of cold pressing the powders and the extrusion process of the green compacts (hereafter designated as 2060 and 2196). The second route consists of cold pressing the powders followed by a heat treatment of the compacts at 525 °C in N_2 pure atmosphere and extrusion processing for both compositions (hereafter designated as 2060HT and 2196HT). The two processing routes followed to produce the rods have been fully described in previous research [17].

Scanning electron microscopy (SEM) was used to characterize the microstructures and study the differences in the extruded products from compacts with and without heat treatment previous to the extrusion process. The samples were prepared using conventional metallographic techniques. The longitudinal and transversal sections were obtained from the middle of each extruded rod. Energy Dispersive X-Ray Analyzer spectroscopy (EDS) was applied to identify the alloying elements. The green compacts and rods were submitted to thermal gravimetric analysis (TGA), which was carried out using a Simultaneous Thermal Analyzer (STA) 6000 from PerkinElmer. STA analysis was performed under a high-purity nitrogen atmosphere (flow rate 20 mL/min) with temperatures ranging from 100 to 800 °C and 5 °C/min of heating rate.

Inductively Coupled Plasma-Optical Emission Spectrometry (ICP-OES), Perkin Elmer Optima 3300DV, and the SPECTRO Arcos model were used for the chemical analysis. Specimens were submitted to the digestion procedure where they were dissolved in an aqueous solution of nitric acid for two days inside an oven at 100°. An intermediate stage of sonication with the addition of hydrogen peroxide was carried out to activate the digestion process of the samples. The measurements were performed in an aqueous solution of 10% nitric acid in duplicate to check the effectiveness of the attack process.

Samples analyzed by EBSD were first prepared using conventional metallographic techniques finishing the mirror-like surface on a vibratory polisher (VibroMet™ 2 Vibratory Polisher, Buehler, USA) with 0.04 μm Struers OPS colloidal silica. EBSD data were analyzed using OIM AnalysisTM software to obtain the orientation maps, inverse pole figures

(IPF), grain size, misorientation and texture. The grain boundary constituents and secondary phases formed were also identified.

Vickers micro-hardness tests (0.5 HV) were also performed by a Zwick Roell micro-hardness instrument (Zwick Roell, DE), and the data were analyzed by the hardness testing software ZHμHD. The tensile test samples were prepared in the extrusion direction according to ASTM-E8/E8M-16a standard. Samples with dimensions of 1.1 mm in thickness and 10 mm in length were produced by machining the rod as shown in Fig. 1. The tensile tests were performed at room temperature in a stress-strain micro-testing machine designed by Microtest. They were performed at a speed of 0.5 mm/min with a preload speed of 0.02 mm/min and a breakage sensitivity of 25% with a maximum load of 5 kN. Fracture surfaces of the samples after the tensile test were examined by SEM.

3. Results and discussion

3.1. Scanning electron microscopy and EDX analysis

To observe the effect of possible microstructural heterogeneities, the microstructures of the rods corresponding to 2060 and 2060HT were studied and can be observed in Fig. 2. Comparing the micrographs of Fig. 2a and b corresponding to the 2060 sample with those of the 2060HT, a lower porosity and higher homogeneity in the 2060HT sample can be noted (Fig. 2 c and d). This can be explained by the fact that during the heat treatment, diffusion mechanisms are activated that promote the bonding of particles as well as a solid solution.

Sparse particles are also observed in Fig. 2a; the EDS analysis reveals that they might correspond to the original Cu particles ($\geq$ 75 at. % Cu) as their size is 15–20 μm, similar to the biggest particles of the original Cu powder. The EDS analysis of four zones of the particle is shown in Fig. 2a in (1) external zone: 33 at. % Cu (2) intermediate zone 1: 51 at. % Cu (3) intermediate zone 2: 60 at. % Cu and (4) internal zone: 98%. at. Cu. Thus, the processing temperature during the extrusion process was not enough to allow diffusion of the alloying elements in the elemental former particles.

Fig. 2 (c, d), corresponding to the 2060 HT sample, also shows these bright sparse particles. Nevertheless, they are smaller and more homogeneously distributed than those found in the 2060 sample (Fig. 2b). The EDS analysis of these bright particles, identified as Al-Cu, and pointed out in Fig. 2c, presents the composition: 26 at. % Cu and 73 at. % Al and is similar to the incoherent and stable θ-(Al_2Cu) phase commonly found in aluminium alloys of a similar composition [18,19]. However, other bright compounds, identified as Al-Cu-Mg, show a composition by EDS of 2 at.% Mg, 16 at.% Cu and 82 at.% Al, which could suggest the formation of S-phase (Al_2CuMg) despite the low at.% of the Mg. Mg was added as a master alloy ($Al_{92.1}$ $Mg_{7.9}$), and the diffusion coefficient of Mg in Al ($3.16{\cdot}10^{-13}$ m^2/s at 525 °C) is higher than that of Cu in Al ($8.06{\cdot}10^{-14}$ m^2/s at 525 °C). Thus, Mg could be homogeneously distributed into the Al matrix and also explains the presence of Mg-rich precipitates through the whole sample. The precipitates of θ-(Al_2Cu) and S-(Al_2CuMg) phases could be formed during the cooling stage, thanks to the diffusion promoted by previous HT and hot extrusion processes [20,21].

In this alloy, AA2060, B. Cai et al. [22] confirmed the predominant presence of two phases: T1 (Al_2CuLi) and θ' (Al_2Cu), and they found that the T1-(AlCuLi) phase could also be formed. However, due to the limitations of FE-SEM with EDS in detecting light elements, such as lithium, there is no direct evidence of these precipitates as reported in the literature. In comparison to 2060 samples, it is clear that the heat treatment of the compacts at 525 °C for 1 h previous to the extrusion process promoted the diffusion of the alloying elements and the precipitations of new phases during subsequent cooling.

Fig. 3 shows the SEM images for 2196 alloy. All the micrographs reveal a higher porosity than that of the 2060 alloy. The dark areas correspond to pores and oxides. This is appreciably different from the previous composition, despite both alloys being processed under the same conditions. Furthermore, the 2196 sample (Fig. 3 (a, b)) shows a higher pore content than 2196HT (Fig. 3 (c, d)). The white particle in Fig. 3a corresponds again to elemental copper particles, which confirms the poor interdiffusion between the Al matrix and alloying elements at this stage for 2196 alloy.

Al-Cu-Mn-rich particles were identified in all the samples (can be seen in Fig. 3 (d)). The EDX analysis was carried out, resulting in 11 at. % Cu, 17 at. % Mn, and 72 at. % Al. Mn is the most critical alloying element and hardly diffuses to form a solid solution with the Al matrix at the temperatures under study according to the consulted phase diagram [17]. Nevertheless, Cu and Al seem to have diffused into former elemental Mn particles, as was reported in previous works [17].

According to these results, heat treatment is a key step in this process. The heat treatment was carried out to promote diffusion in a nitrogen atmosphere. Nitrogen has an active role in the aluminium alloys processing [23], since aluminium forms a stable oxide layer which limits diffusion and densification [24]. G. B. Schaffer and B. J. Hall have demonstrated that during heating, the oxide layer grows, decreasing the oxygen partial pressure in the gas as it travels into the pore network [25]. In the deep pore network, where the gas flow rate is much lower than on the surface, the oxygen may be consumed by the aluminium faster than it can be replenished by the incoming gas. The local partial pressure of oxygen will then reduce and the aluminium acts as a self-getter. At this moment, thermal expansion may cause the oxide layer to fracture. These fractures will readily heal when oxygen is present. However, the oxide will not heal when the oxygen concentration is reduced by self-gettering, leading to the formation of AlN, aiding the sintering [25]. Thus, when Al is heat treated under a nitrogen atmosphere, the formation of AlN promotes the densification by the reaction of aluminium with nitrogen according to $Al + N \rightarrow AlN$. Although there is no evidence for formation of AlN, all samples heat treated in nitrogen before the extrusion process showed a reduction in pore size as can be seen in the figures shown above.

According to other studies [26–28], the presence of Mg in aluminium alloys is also key in the bonding process of the Al powder particles. The addition of small amounts of Mg shows that it reacts with the Al_2O_3 film to form the $MgAl_2O_4$ spinel [26], breaking the oxide, exposing the

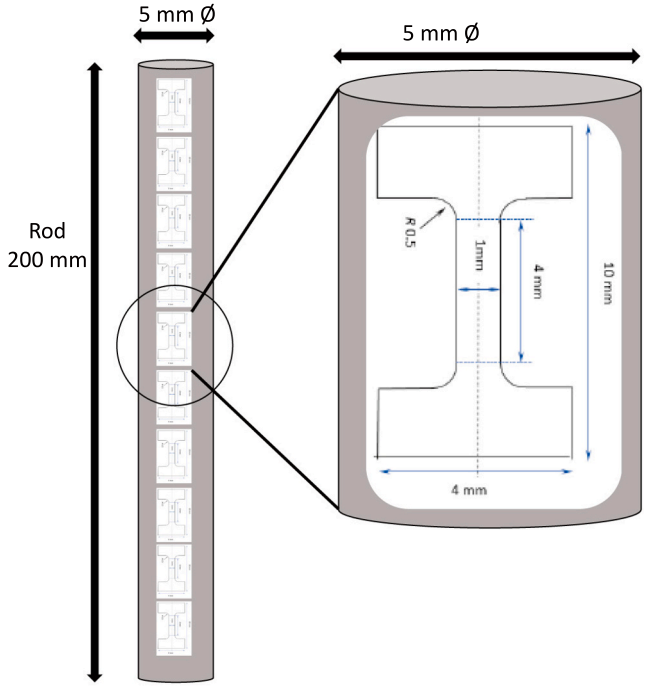

Fig. 1. Schematic drawing of tensile test samples.

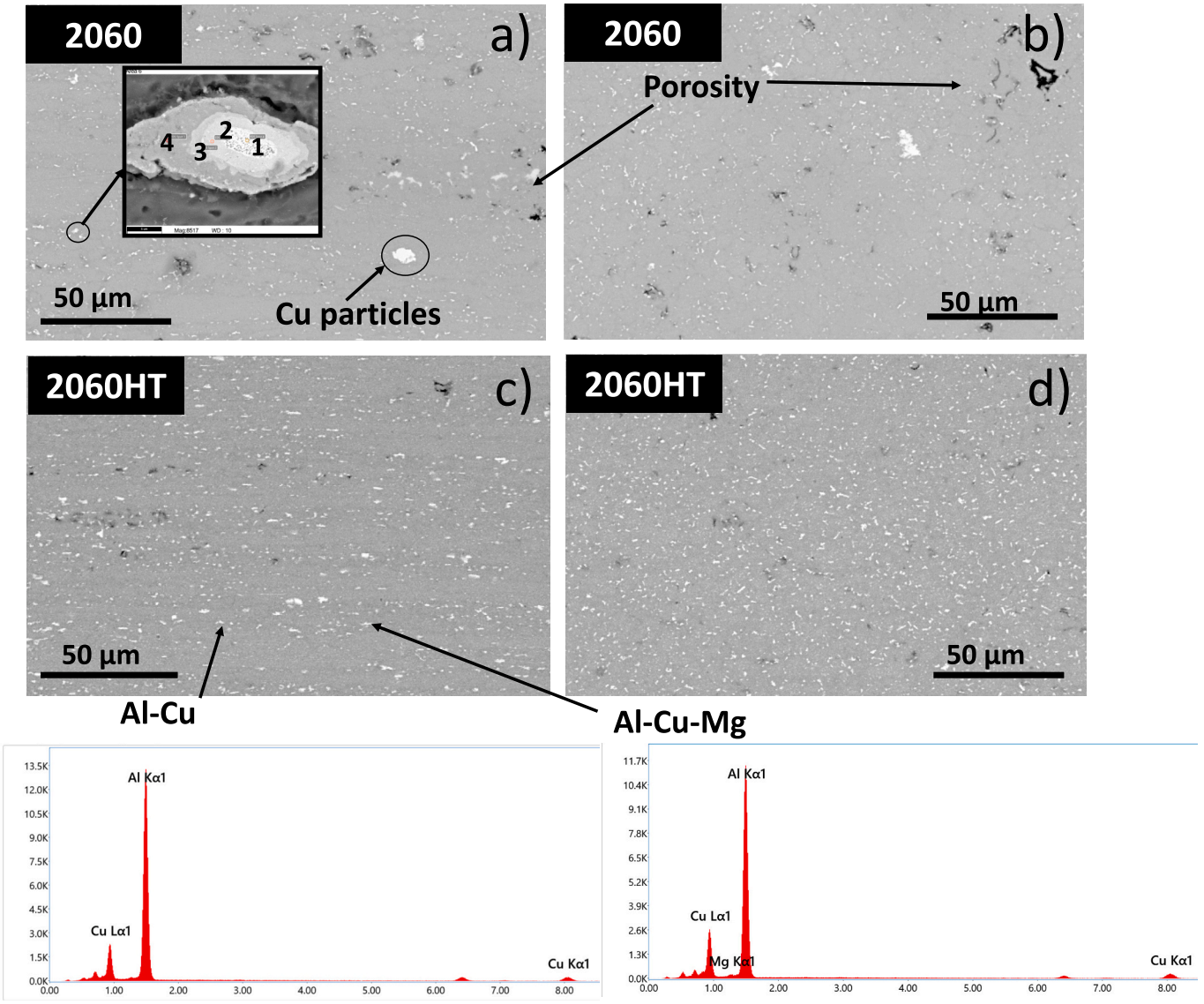

Fig. 2. SEM images of the 2060 alloy rods extruded without (a, b) and with (c, d) heat treatment (HT) prior to extrusion, showing longitudinal section (a, c) and cross-section (b, d).

underlying metal and facilitating the sintering process [24]. The significant difference in the Mg content of both alloys, 0.85 wt% for the 2060 alloy compared to 0.35 wt% for the 2196, could explain the differences found in the porosity.

Several TGA measurements under different conditions were performed to understand the behavior and affinity of compacts with pure N_2 and air atmospheres along the different steps of the production routes. The first test was performed with the green compacts in the N_2 atmosphere to reproduce the heat treatment conditions. The second test was performed with all the compacts, without and with HT, in the air (21% O_2 79% N_2 by volume), to understand the affinity of the compacts when they are extruded in the lab.

In Fig. 4a for TGA-Nitrogen a significant difference can be seen in the behavior of both alloys, showing a substantial mass gain with temperature for the 2060 alloy related to good interaction between that alloy and N_2. A similar behavior should be expected for 2196 alloy since they are both Al alloys, however, the differences may be due to the alloying elements, particularly in Mg content.

During the extrusion process at 525 °C in the air atmosphere (Fig. 4b), the different slopes show that 2060 alloy presents a higher tendency to react with some elements of the atmosphere than 2060HT. Therefore, the extrusion process of 2060HT seems to be the most favorable, resulting in a better diffusion of alloying elements and densification of the material.

Conversely, a decrease is observed in the slope of the mass-gain curve for the 2196 alloy (Fig. 4a). The mass loss for 2196 relates to the sublimation of some elements and the lack of reaction between N_2 and the sample. This factor and the low Mg content can explain the results of the microstructure of 2196 alloys, although 2196HT had a higher tendency to react with the atmosphere during air extrusion of the compacts than 2196 (Fig. 4b).

3.2. Optical emission spectrometers with excitation source ICP (ICP-OES)

The chemical analysis was performed to quantify the loss of alloying elements during the process since the high temperature in both solid-state processes can lead to the sublimation of some of the alloying elements. Three areas of the rod were analyzed: top, middle, and bottom. No composition differences were observed, and it was concluded that the composition is homogeneous through the extruded rods for samples without and with previous HT. Therefore, the average values obtained were calculated and the quantitative analysis is shown in Fig. 5, where

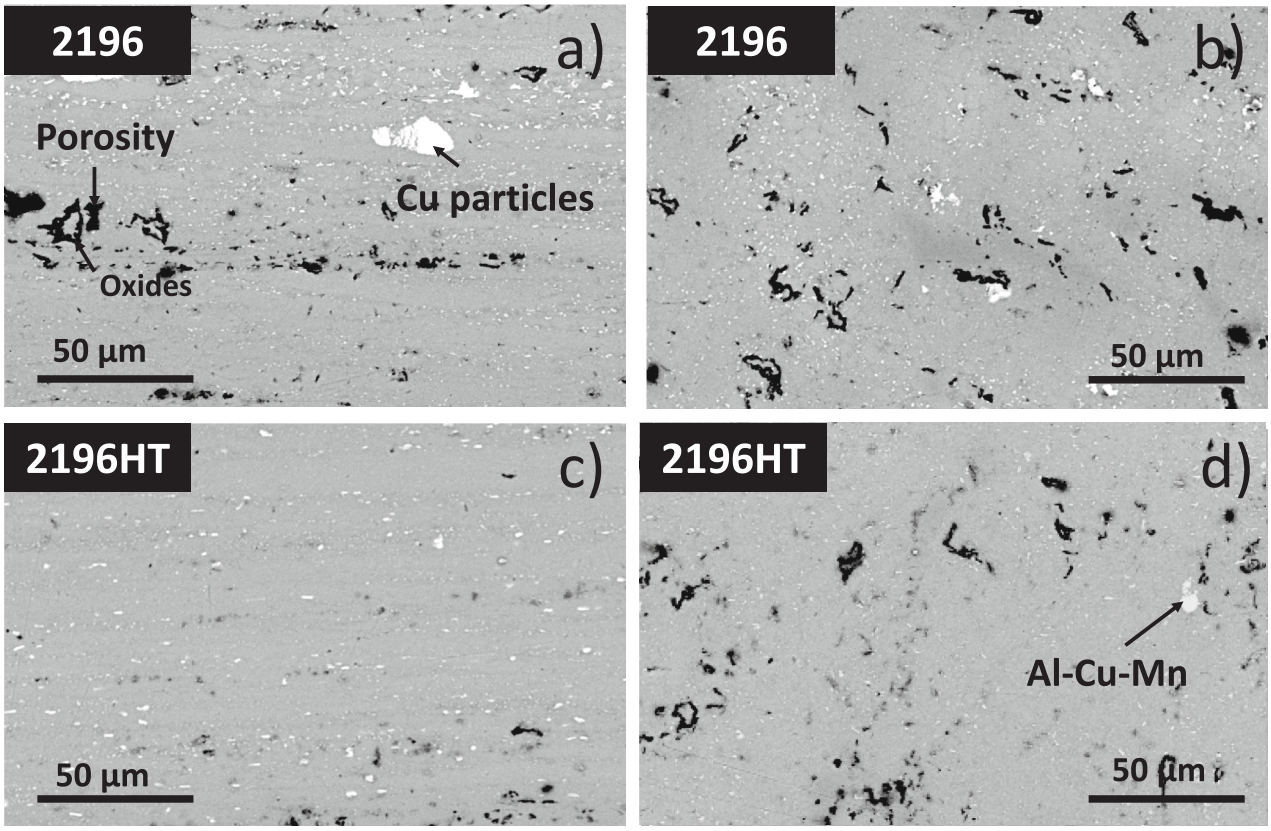

Fig. 3. SEM images of the 2196 alloy rods extruded without (a, b) and with (c, d) heat treatment (HT) prior to extrusion, showing longitudinal section (a, c) and cross-section (b, d).

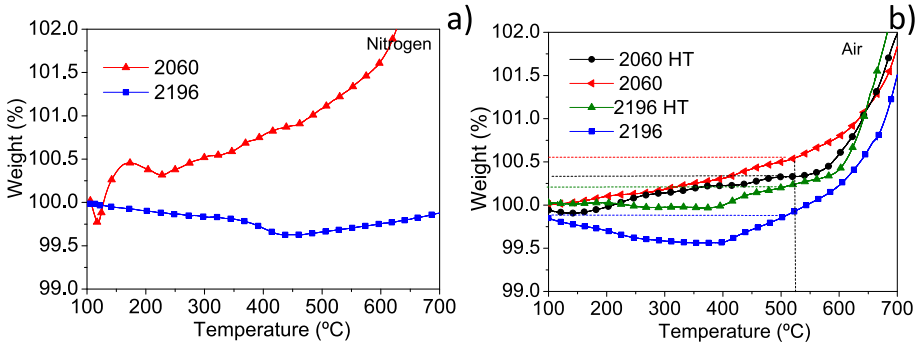

Fig. 4. (a) TGA of the green compacts before the extrusion process in the nitrogen atmosphere (b) in the air atmosphere. (For interpretation of the references to color in this figure legend, the reader is referred to the web version of this article.)

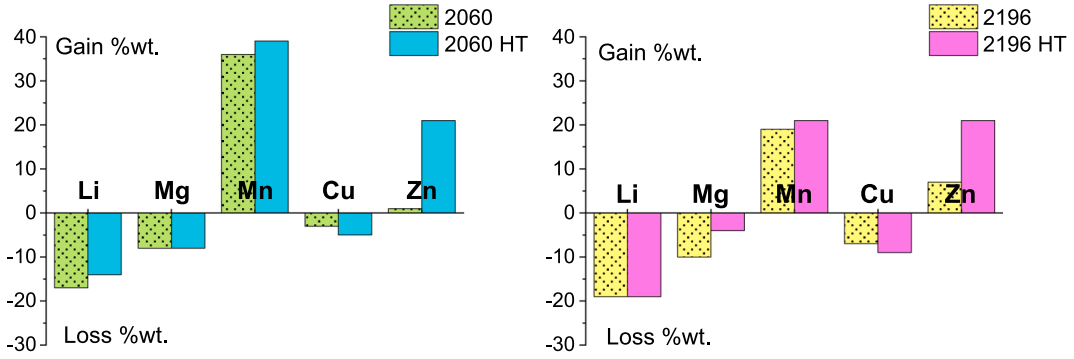

Fig. 5. Weight loss and gain percentage of the alloying elements after the extrusion process for both alloys.

the percentage of loss and gain with respect to the initial weight is expressed.

The loss of lithium, magnesium, and copper are related, in that order, to the volatility of the alloying elements. The vapor pressure varies according to Li > Mg > Cu [29]; the higher the vapor pressure, the higher the volatility. The values show less loss for HT materials because during heat treatment all the diffusion phenomena are promoted, helping the dissolution of the alloying element in the Al matrix. In addition, the surface area of the compact is reduced, which finally hinders the loss of volatile elements.

On the other hand, gains in the alloying elements of Mn and Zn are observed, although they are not fully understood. One possible explanation for Zn gain can be that zinc stearate has been used as a lubricant in the green compact from the pressing step before the extrusion process. Zinc stearate is believed to not contaminate metals because of its burning temperature (300–400 °C) [30] but some particles may be trapped. Zinc carbide may be formed by the pyrolytic decomposition of zinc stearate. Consequently, the chemical composition results are altered if zinc penetrates inside the compact. No explanation can be found in the gain of Mn except that resulting from the heterogenous Mn distribution through the material due to poor diffusion of this element in the Al matrix.

3.3. Evolution of microstructure: EBSD

EBSD measurements were performed to obtain the grain orientation and grain size distribution, as well as the texture present in the studied materials. OIM maps (Orientation Imaging Microscopy), following the Inverse pole figures (IPF) color scheme, were generated from the analysis of the EBSD data to study the evolution of the microstructures after the hot extrusion process.

OIM maps of the transversal section are shown in Fig. 6, where the black line represents grain boundaries with a misorientation angle above 15°, which correspond to high-angle grain boundaries (HAGB), and the white lines represent subgrain boundaries with a misorientation angle between 5 and 15° (low-angle grain boundary, LAGB). The presence of texture in the materials, especially for the 2060HT (see Fig. 6), is clearly observed from the high-density number of blue grains, which corresponds to the texture of grains associated with ⟨111⟩ fiber. For the four studied alloys, the shape of the cross-section of the grains is equiaxial in this plane, as is observed in Fig. 6 (a)-(d).

The corresponding images of the longitudinal section are shown in Fig. 7. They reveal the elongated shape of the grains with their major axe along the extrusion direction, without a clear dominant crystallographic orientation.

From Figs. 6 and 7, it can be deduced that heating during the extrusion process has produced texture materials with partially recrystallized microstructure, although the presence of some non-fully recrystallized grains are observed (see for example, the sub-grain boundaries marked with black arrows in Fig. 7).

In the Fig. 7, all images show regions of small grains and larger grains oriented in the direction of extrusion, and there is no difference between the four conditions. Published studies demonstrate that small additions of alloying elements, such as Zr, Zn, Sc, Ti, and Li, minimize the degree of recrystallization and improve mechanical properties by forming a fine and coherent phase (Al3X) [31–33].

The average difference in orientation between each pixel inside a grain and the grain orientation average is used to calculate the grain orientation spread (GOS). GOS levels are lower in recrystallized grains than in deformed grains [34–36]. The GOS distributions of all the samples are compared in Fig. 8.

In this work, a threshold value of 3° was chosen to distinguish recrystallized and non-recrystallized grains [34,37]. This threshold value is determined to distinguish a fully-recrystallized grain from a recovered one, which implies that grains with GOS < 3° are recrystallized. In a GOS map, all pixels within a grain are shaded with the same color depending on the threshold value. The blue grains are the completely recrystallized grains, while some of the orange or red grains can be considered partially crystallized or non-recrystallized.

Fig. 8 compares the grain orientation spread distributions obtained for the analysis of the GOS-Mas presented in Fig. 9 for all the produced alloys. A systematic trend of the reduction in the GOS value for 2060,

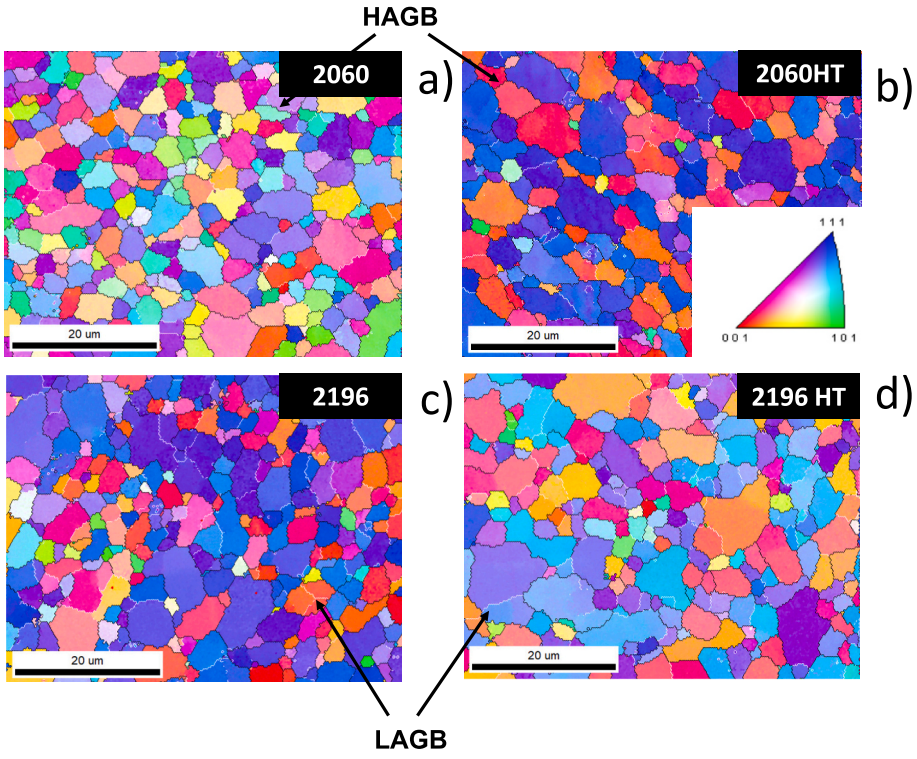

Fig. 6. OIM maps of cross-sections of the extruded rods: (a) 2060 (b) 2060HT (c) 2196 and (d) 2196HT.

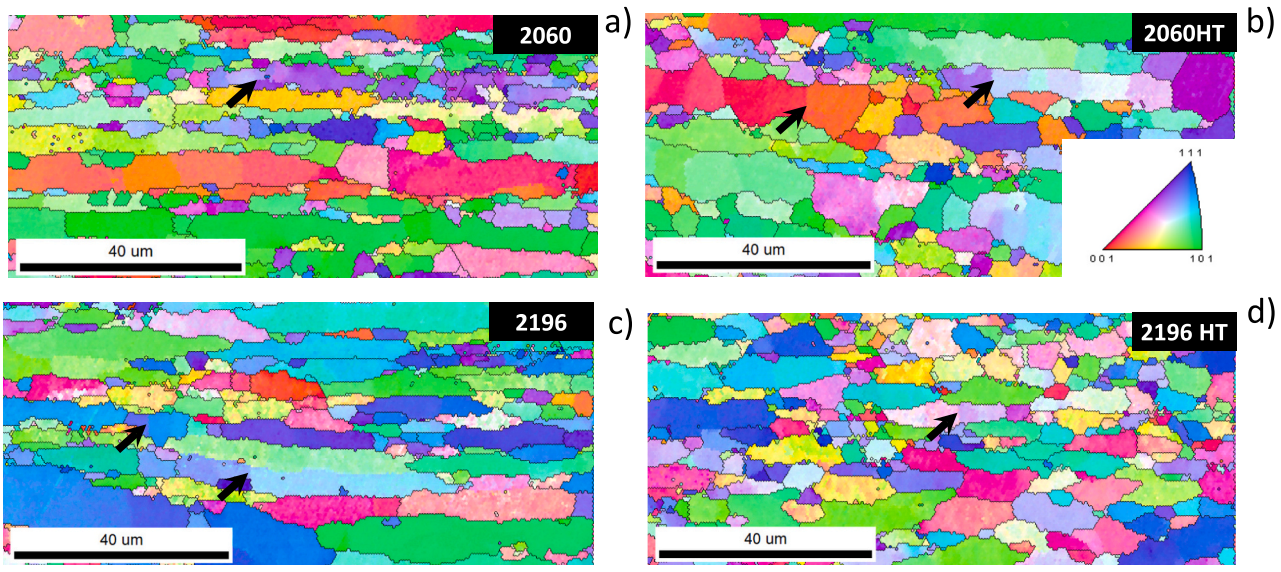

Fig. 7. IPF-Maps of the extruded rods, longitudinal sections (a) 2060 (b) 2060HT (c) 2196 (d) 2196HT. Black arrows point to non-fully recrystallized grains.

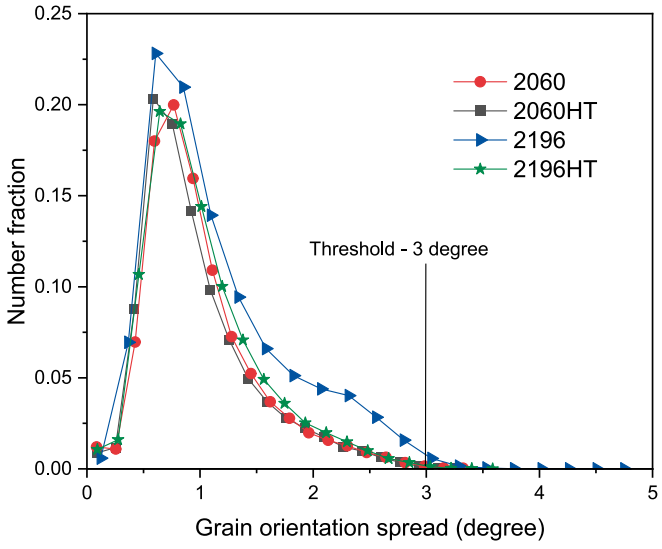

Fig. 8. Grain orientation spread (GOS) distributions. The red line at 3° marks the threshold between recovered and recrystallized grains. (For interpretation of the references to color in this figure legend, the reader is referred to the web version of this article.)

2060HT and 2196HT can be observed, indicating progress in microstructure restoration.

The GOS-Maps presented in Fig. 9 clearly show that the number of recrystallized grains is higher for the 2060 HT and 2196HT materials. However, the maximum value of 5° is observed for all the cases, which corresponds to a low value of the mean intragranular misorientation, indicating that a high degree of recrystallization has been achieved through recrystallization processes at extrusion.

Fig. 10 shows the grain size distribution histograms obtained from the analysis of the EBSD measurements on the cross-sections, using 5° as a minimum grain boundary reconstruction angle. The samples without HT before the extrusion process (2060 and 2196) show smaller sizes of their cross-section perpendicular to the extrusion direction compared with HT samples (2060HT and 2196HT). Furthermore, the grain size of 2196 and 2196HT shows a larger distribution compared to 2060 and 2060HT.

In addition, the grain size was measured in the longitudinal section* (*This grain size should be understood as the diameter of the circle with an area equivalent to the grain area). The average grain sizes for the 2060 and 2060HT samples were 10.6 μm and 8.8 μm, while the 2196 and 2196HT exhibited average grain sizes of 14 μm and 8.4 μm, respectively. The samples with HT (2060HT and 2196HT) show smaller grain sizes as compared with the sample without HT (2060 and 2196).

The grain boundary misorientation distribution (GBMD), or intergranular misorientation, was calculated for all the materials. The frequency distribution histograms obtained for the misorientation angle along the grain boundaries, showing the intergranular misorientation of the four conditions, are depicted in Fig. 11. As a reference, the ideal standard MacKenzie distribution of untextured equivalent alloy is presented, which corresponds to a material with randomly orientated grains (see subfigure 11-(a)).

The results reveal that the alloys have partially recrystallized following a distribution similar to the random misorientation characterized by the MacKenzie distribution for a cubic structure [38–40]. However, the MacKenzie distribution has its maximum value at 45°, while the maximum of the GBMD is shifted towards higher angle values for all the studied materials. This shift, together with the overall shape of the GBMD, agrees with the presence of a recrystallized texture in the materials associated to the presence of a ⟨111⟩ fiber texture [41,42]. The other possibility, that the shift was caused by the presence of significant density of inter-variant boundaries or CSL (Coincidence Site Lattice) boundaries, has been discarded for these alloys. Thus, the presence of high values of a peak at angle values higher than 45° is consistent with a stronger fiber texture and, therefore, it is expected that the 2196HT presents the strongest texture components in the pole figures, while the non-heat-treated should present a weaker texture.

Fig. 12 shows the grain boundary misorientation angle along the grain boundaries. It can be clearly observed that the microstructure corresponds to a material where more of the grain boundaries present HAGB. In addition, these maps indicate that hot extrusion results in increased local deformation throughout the samples and the accumulation of deformation occurs at the grain boundaries, showing grain boundaries that are predominantly red.

To obtain the texture components of the extruded alloys and their intensities, the pole figs. (PF) were derived from the EBSD measurements on samples in the cross-section (see Fig. 14), corresponding to the surface of the sample in a direction perpendicular to ED and TD, as indicated in the scheme of Fig. 13. According to Fig. 13a, which represented the extruded products, the pole figure of the cross- sections would

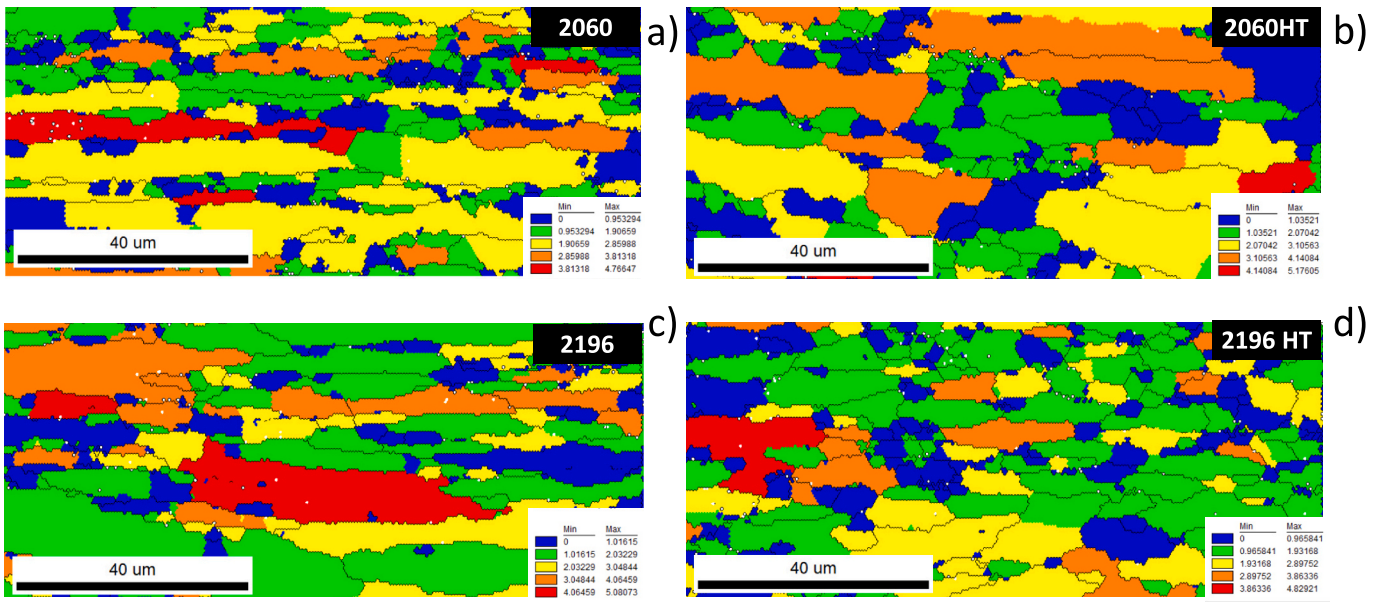

Fig. 9. GOS-Maps of the extruded rods, longitudinal sections (a) 2060 (b) 2060HT (c) 2196 (d) 2196HT.

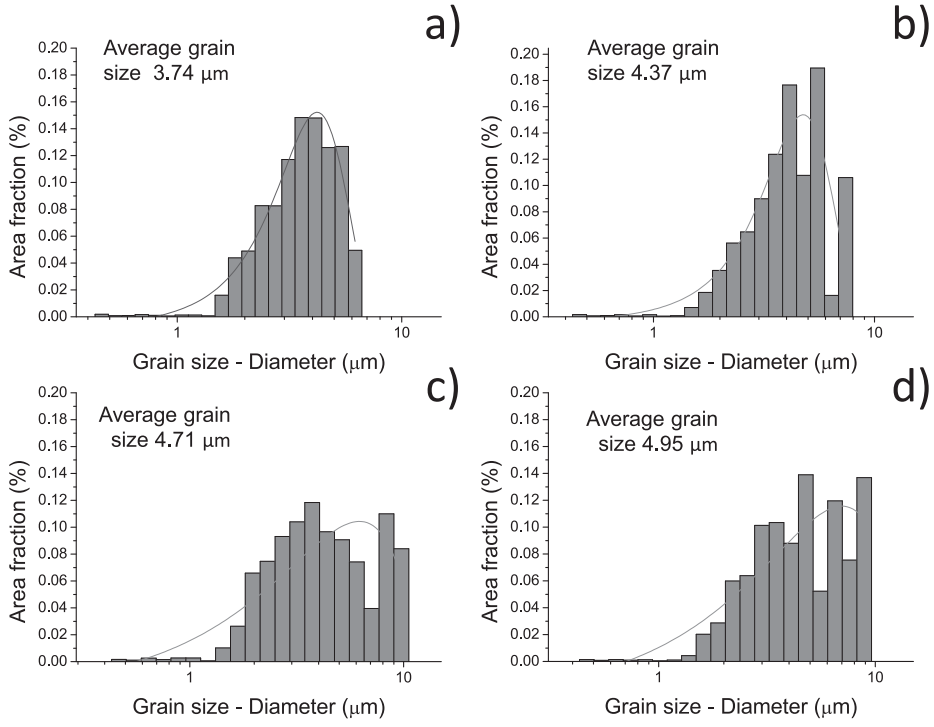

Fig. 10. Grain size distributions of (a) 2060 (b) 2060HT (c) 2196 and (d) 2196HT.

be presented as Fig. 13b with respect to the laboratory reference system.

The shape and texture of the grains change via grain rotation and subdivision during the extrusion processing due to plastic deformation. This produces changes in the relative orientations of the grains favoring some specific orientations with respect to the extrusion direction, which can produce the formation of texture. When the texture is present, the pole densities will be stronger around some preferred specific orientations compared with the expected one for an untextured material with randomly orientated grains.

The analysis of the (001), (110) and (111) pole figures of the alloys presented in Fig. 14 reveals the presence of similar texture components for all them, whereas differences in the strength of the texture components are observed.

The maximum values of intensity are obtained for 2060 and 2196, 8.5 mrd and 14.0 mrd respectively, compared with values obtained for the heat-treated samples, 2060HT and 2196HT, of 13.341 mrd and 15.150 mrd, respectively. This shows the same tendency observed in Fig. 11, where the highest values of misorientation angles were obtained for HT materials. The texture of the 2060, with a maximum intensity of 8.532 mrd, is significantly weaker than the rest. This result agrees with the shape and the position of the maximum value observed in the GBMD histograms of Fig. 10.

The analyses of the pole figures show that the preferential orientation of the grains presents two main components, which correspond to

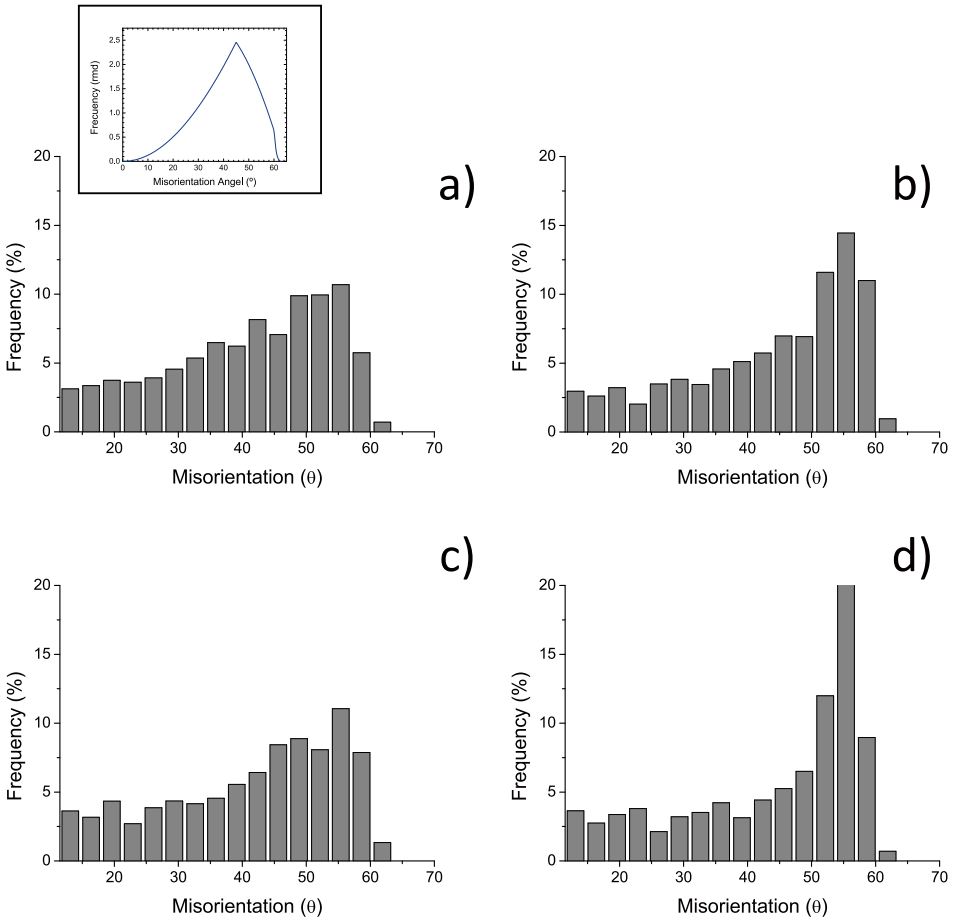

Fig. 11. Misorientation distribution of (a) 2060 (b) 2060HT (c) 2196 and (d) 2196HT. Subfigure a) depicts the expected distribution of misorientation angles for textureless cubic polycrystals.

the ⟨001⟩ and < 111> fibers, i.e. the planes are directly parallel to the extrusion direction. The rings around the center are secondary rings that often coincide with planes equivalent to the one depicted. For example, for a < 111> fiber texture, a secondary ring should appear at 70.5° on the pole figure. And for a ⟨001⟩ fiber texture, there should be a ring at 90° on the pole figure. Another factor is the phenomenon of ring blurring, which is present in all conditions and is characteristic of <001> and < 111> pole figures and related to a certain change in grain orientation. Thus, the consequence is a slightly inclined 110 pole. A slight weakening of the texture after recrystallization is observed as well in PF <001> for 2196 (Fig. 14c).

To determine which of the preferential directions is more significant, and therefore more preferential, the volume fraction has been calculated from the crystal direction map (Fig. 15), with a tolerance value of 10° for the three directions. The crystal direction map represents the fraction of material that has a particular crystal direction aligned with a reference sample.

For the 2060HT and 2196 samples, both the pole plot and the standard texture analysis show the texture of the material dominated by <111> fiber. The volume fraction values indicate that the material is largely oriented towards direction <111>, but a significant volume fraction of the material is made up of grains that are oriented towards direction <001>. Thus, the deformation texture is a strong <111> and weak <001> duplex texture.

Although the pole figure (Fig. 14) also indicates two preferential directions <001> and < 111> for the 2060 and 2196HT materials, these materials are less oriented, and their texture is weaker compared to the 2060HT and 2196 materials. These results also agree with the IPF images (Fig. 6), in which 2060 and 2196HT showed less intense and lighter colors in their cross-sections, evidencing a less pronounced orientation.

In conclusion, the samples show typical double <001>Al//ED and < 111>Al//ED axisymmetric deformation texture components under all conditions. Furthermore, in fcc metals the typical texture due to drawing and extrusion processes produces <111> + ⟨100⟩ duplex, both parallel to the extrusion direction [43]. The texture in direction <111> is shown as the most intense direction for the 2060HT and 2196 samples.

3.4. Vickers micro-hardness tests

Hardness measurements were carried out on the compacts before being extruded, as well as on the extruded rods, for a complete characterization since the extrusion process requires a force that depends on the resistance of the material to flow.

The hardness is shown in Fig. 16. For 2060 alloy, it can be seen that the heat treatment slightly increases the hardness of the compact. The contrary is observed for 2196 alloy: heat-treated compacts show lower hardness than those without green compacts. 2060 alloy presents higher copper content, which promotes the formation of phases T1 (Al_2CuLi) and θ'(Al_2Cu) [44]. The presence of these phases after heat treatment could explain the strengthening of this alloy more than the 2196 alloy, which contains lower Cu content and higher lithium. The hardness of the 2196 and 2196HT compacts are very close and lower than the 2060 alloy. Comparing the hardness values of both alloys, 2060HT and 2196HT, the latter one is lower, probably due to the porosity and non-suitable heat treatment. The difference for both alloys in Mg content, 0.85% wt. for 2060 alloy and 0.5% wt. for 2196 alloy, can also contribute to the difference in hardness. As mentioned, Mg increases resistance by strengthening the alloy.

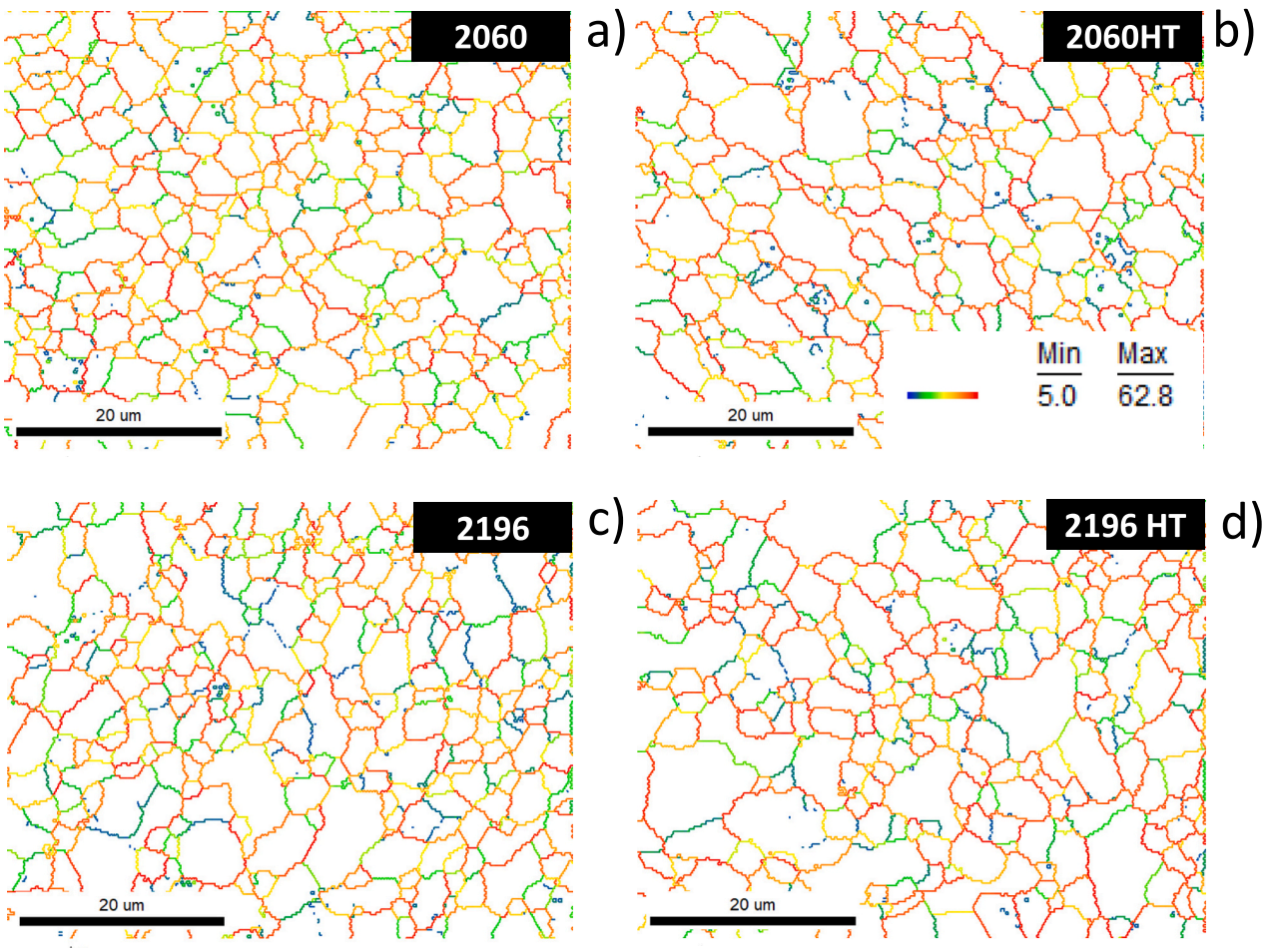

Fig. 12. Local Average Misorientation (LAM) maps of (a) 2060 (b) 2060HT (c) 2196 (d) 2196HT.

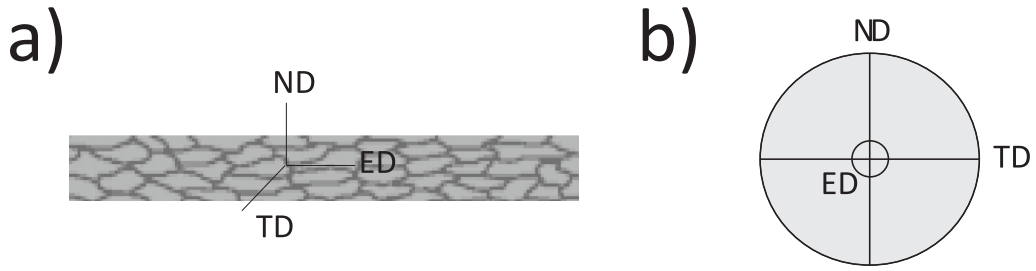

Fig. 13. Scheme of the selected directions (a) drawing of the rod and its directions (b) representation of the direction on the pole fig. ED: extrusion direction, ND: normal direction perpendicular to the surface of the sample and ED, and TD: perpendicular to de ND and TD.

The extrusion process provides extruded rods with better mechanical properties due to the solid-state deformation process and high temperature. It can be seen from Fig. 16 that hardness is increased in all the extruded rods regardless of the composition or conditions.

The results in the hardness for the 2060 alloy can be explained by the fact that the heating previous to the extrusion promotes the dissolution of alloying elements. A more homogeneous and hardened alloy makes the extrusion more difficult while the formation of precipitates is being produced during cooling after extrusion. Thus, significant changes are observed between the 2060 green compact (59 HV) and the 2060 extruded rod (98 HV). The 2060 rod is hardened by the strain and precipitation hardening effects.

Nevertheless, 2060HT has been previously dissolved and precipitated during the cooling of HT. Heat treatment previous to extrusion probably leads to the dissolution of some precipitates and the growth of others, which reduces elements in solid solution and could make extrusion easier, leading to a softer extruded rod. This can be coherent with the microstructures shown above in Fig. 2, where the presence of precipitates in HT samples is higher. In this way, strain hardening is the dominant hardening mechanism. The 2060HT compact is 65 HV, while 2060HT extruded rod is 89 HV.

The 2196 alloy shows the lowest hardness values due to the presence of a high number of pores in the microstructure. In this case, comparing compacts and extruded rods, the benefits of the deformation caused by the solid-state hot extrusion lead to a strong reduction in porosity and produce significant benefits in hardness regardless of the conditions.

3.5. Tensile test

Fig. 17 shows the engineering strain-stress curves for the material

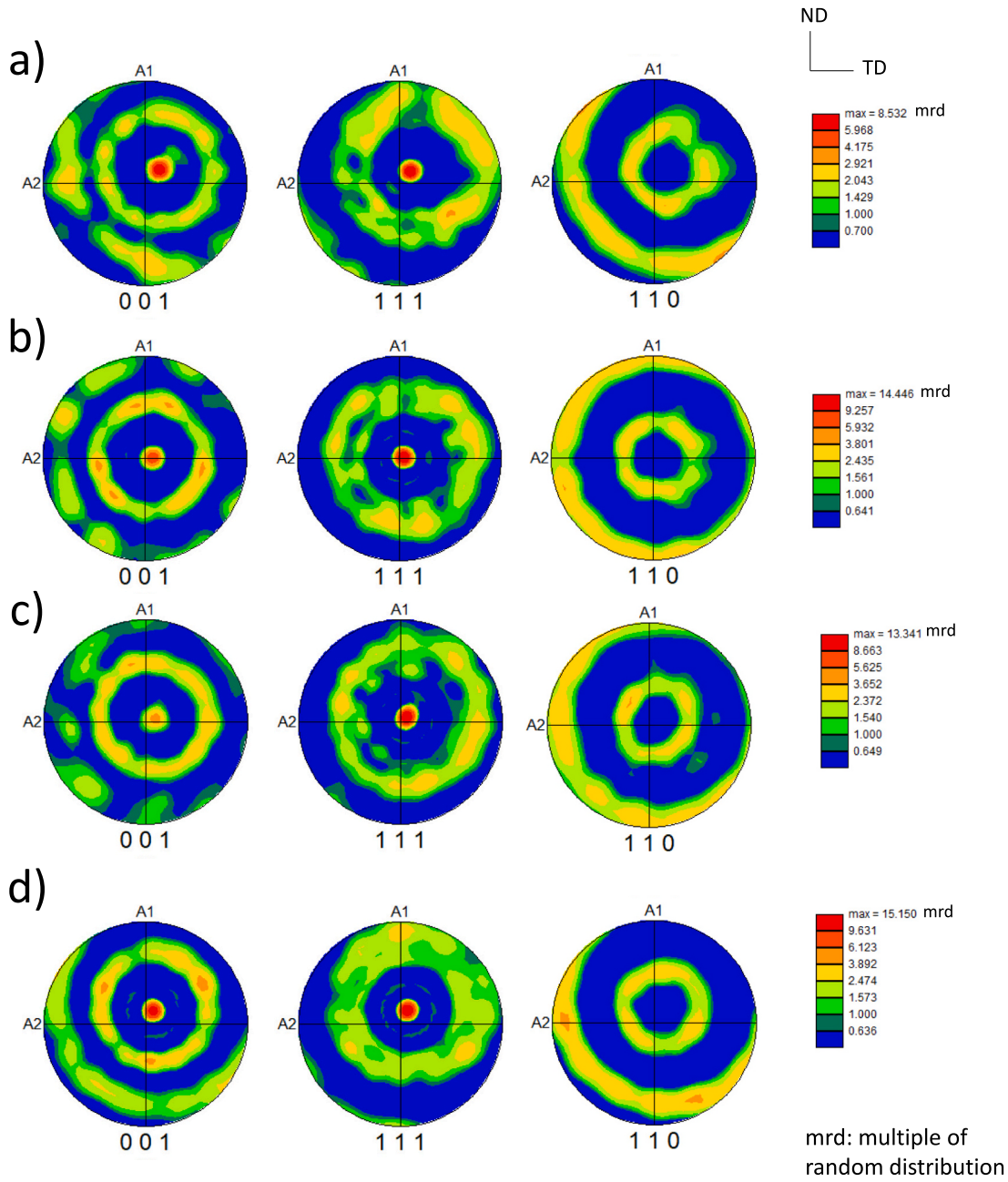

Fig. 14. Representative pole figures of (a) 2060 (b) 2060HT (c) 2196 (d) 2196HT.

after extrusion. From their analysis the tensile characteristics were obtained, showing that that the yield strength values for all the materials were found between 220 and 260 MPa, the ultimate tensile strength values were between 310 and 360 MPa (Fig. 17b), and the elongation between 9 and 15%. Results from other studies showed that the mechanical properties, in particular for 2024 and 7075 extruded alloys [45–47] were found between 158 and 236 MPa for yield strength and 304–345 MPa for ultimate tensile strength. These results are similar or even better than those in the literature, which confirm the suitability of the proposed production routes. This is very important since it must be taken into account that the processing has been carried out using powder metallurgical routes, considering it to be a suitable processing alternative for the consolidation of these alloys.

However, the elongation from other studies showed between 13 and 18.5%, being no >15% in the alloys studied. The 2060 alloy, despite the high hardness results, shows a greater elongation than that of the 2196 alloy. This can be due to the more homogeneous microstructure and the absence of porosity. In addition, the presence of more high-angle grain boundaries (in IPF images Fig. 6) gives the alloy a clear ability to regulate plastic deformation on the grain boundaries and, as a result, the ductility of the alloy improves [48].

The fracture surfaces for the alloys are shown in Figs. 18 and 19. According to these images, all the fractures appear to be ductile, since dimples are observed in all the fracture surfaces, which is common in aluminium alloys. All the dimples are oriented towards the applied stress, with the dimples for the 2060 alloy being slightly more developed than those in the 2196 alloy. A transgranular fracture can also be observed for both conditions in some areas (2060 and 2060HT). Transgranular fracture is caused by the presence of large brittle particles that promote crack propagation, the fracture travels through the grain of the material (Fig. 18 (a,c) -2060) [49]. These particles are large and randomly distributed throughout the material.

The compositional analysis by EDS of the larger particles seen in Fig. 18e for the 2060HT alloy (area 1) show that they are rich in Al, Cu

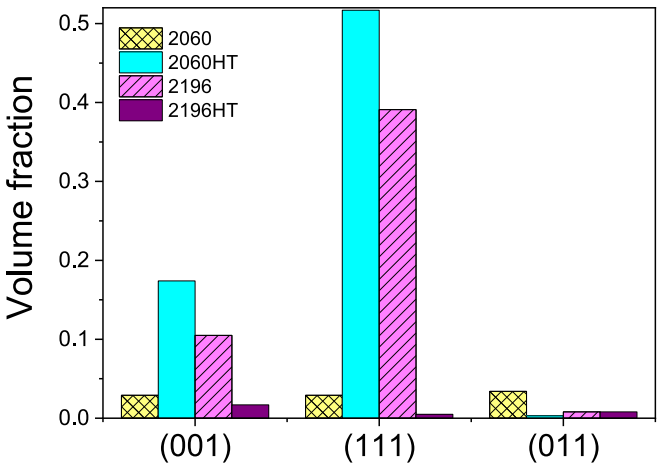

Fig. 15. Volume fraction values obtained from crystal direction plot.

and Mn, corresponding to the Mn-rich particles observed in the microstructure; the EDS analysis of the bright area 2 (Fig. 18g - 2060HT) reveals the presence of Cu, Mg, Al and O, results consistent with the presence of precipitates with compositions such as Al_2Cu and Al-Cu-Mg, which were observed in SEM-EDS in Fig. 3.

The first inspection of the fractography of 2196 alloy reveals, like the 2060 alloy, dimples on the fracture surface, with large-sized particles also being identified. The alloying elements identified for them by EDS were 4 at. % Cu, 20 at. % Mn and 76 at. % Al (Fig. 19a - 2196). Furthermore, small areas rich in Cu, Mg, Al and O are also observed (Fig. 19c-2196). EDS analysis reveals that these precipitates present a chemical composition similar to those of 2060 alloy. In summary, large-sized particles appear on the fracture surfaces in both alloys. This could indicate that these Al-Cu-Mn particles promote the transgranular fracture. The fracture could begin in these brittle particles and advance through the void nucleation produced by the ductile fracture typical of aluminium alloys.

4. Conclusions

In the present study, the influence of chemical composition (high Cu, low Li for 2060 and low Cu, high Li for 2196), the effects of the homogenization, and its properties have been studied, for the aluminium alloys produced following two novel powder metallurgy routes, obtaining promising results for the fabrication of high-strength extruded aluminium alloys for the subsequent production of the wires. After pressing and hot extrusion of the 2060 alloy, it has been possible to obtain rods without porosity and with a homogeneous microstructure. It has been also possible to observe the benefit of Mg addition, which is improved after the HT of the alloys. However, after processing by hot extrusion, 2196 alloy presents a microstructure with a higher level of porosity, probably due to the volatilization of Li. The EBSD analysis showed that all the materials exhibit texture, and a preferential orientation along <100> and < 111> directions, typical of a duplex fiber texture. In addition, HT alloys present slightly more equiaxial grains; the

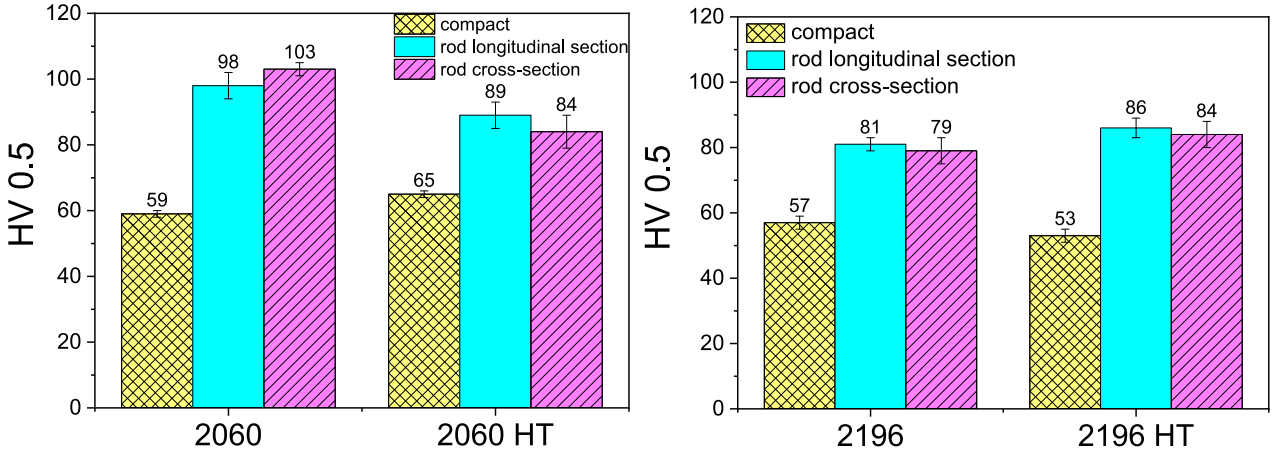

Fig. 16. Microhardness for 2060 and 2196 alloys compacts and extruded rods.

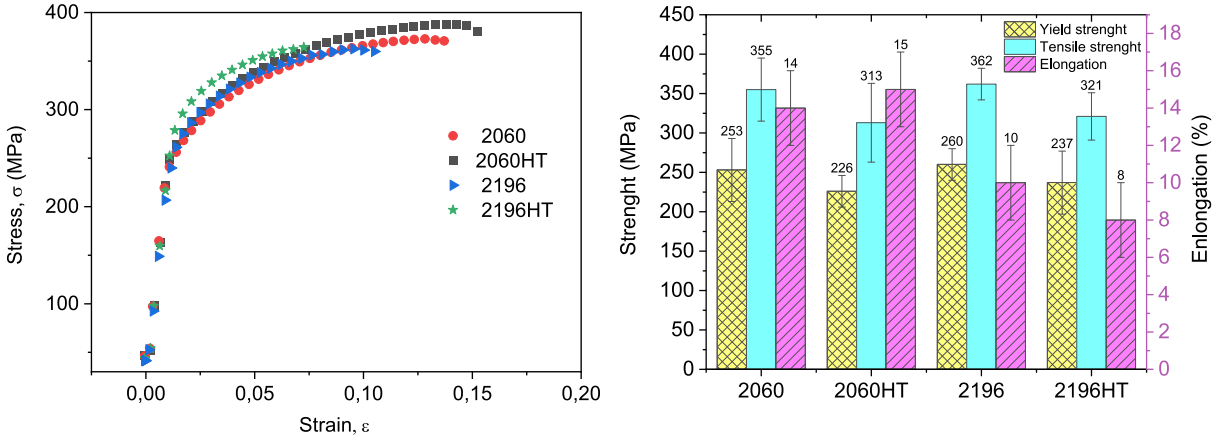

Fig. 17. Stress-strain curve and bar graph of values obtained.

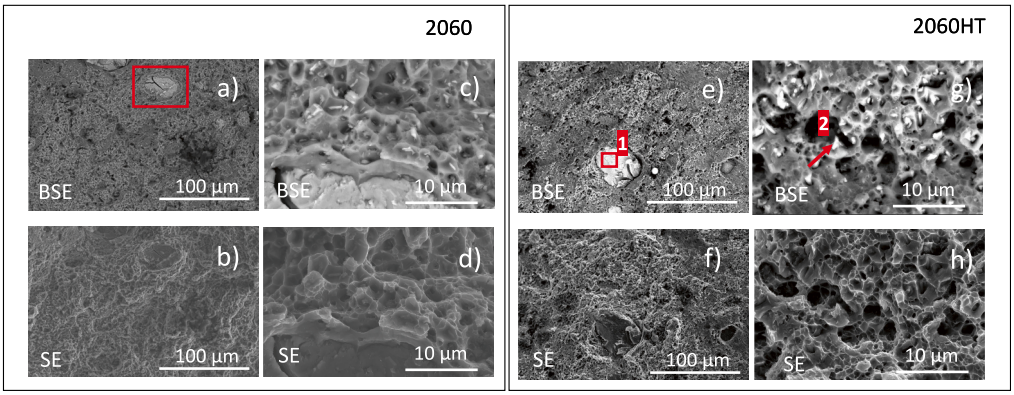

Fig. 18. Image of the fracture surface (a, b, e, f) and magnified images (c, d, g,h) for 2060 and 2060HT alloy.

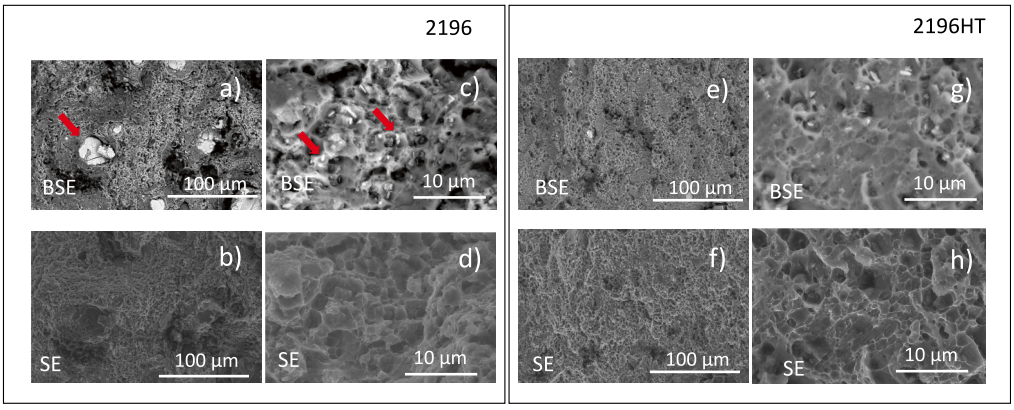

Fig. 19. Image of the fracture surface (a, b, e, f) and magnified images (c, d, g, h) for 2196 and 2196HT.

deformed grains with HT present higher grain sizes in the cross-section and lower ones in the longitudinal section than those without HT. The ICP-OES analysis reports losses of Li and Mg for both alloys, being higher for 2196 alloy than for 2060 alloy, according to the lack of diffusion of the alloying elements found in the microstructure of this first one. The losses of Cu were lower compared to Li and Mg. The hardness values showed by 2060HT alloy are higher than those obtained for 2196HT due to the major homogenization of the alloying elements in the microstructure. The 2060 rod is hardened by strain and precipitation hardening phenomena, while 2060HT appears to be mainly hardened by deformation. The 2196 alloy showed low hardness values due to the presence of a high number of pores in the microstructure. The slightly increased hardness values of 2196HT are probably due to the benefit of reduced porosity derived from the hot extrusion process. Finally, tensile tests showed better ductility for 2060 alloy due to the more homogeneous microstructure compared to that of the 2196 alloy. The lower ductility values obtained for 2196 alloy are also related to the high porosity found in the microstructure.

Financial interests

These may include but are not limited to membership, employment, consultancies, stocks/shares ownership; honoraria; grants or other funding; paid expert testimony and patent-licensing arrangements. Some examples are as follows:

- An author has received or expects to receive research grants from funding agencies (please provide details regarding the research funder and the grant number).
- An author has received support from commercial sources of funding by companies that sell drugs, medical devices, or provide medical services.
- An author has received honoraria for speaking at symposia.
- An author holds a position on advisory boards.
- An author is an inventor of any planned, pending, or awarded patent on this work (please provide detailed information such as regarding the patent applicant, name of inventors, application number, status of application, specific aspects of manuscripts covered in the patent application).
- An author is an employee of an organization or company.

Non-financial interests

These may include but are not limited to personal relationships or competing interests directly or indirectly tied to this research, or professional interests or personal beliefs that may influence your research.

The authors whose names are listed immediately below certify that they have NO conflicts of interest to declare:

Paula Rodriguez-Gonzalez, Elisa Maria Ruiz Navas, Elena Gordo, Miguel Angel Monge.

Funding

Funding for APC: Universidad Carlos III de Madrid (Read & Publish Agreement CRUE-CSIC 2023). The payment for the publication of the article has been accepted by the university and they require us to mention their contribution.

Declaration of Competing Interest

The authors declare the following financial interests/personal relationships which may be considered as potential competing interests:

Paula Rodriguez Gonzalez reports financial support was provided by

the Regional Government of Madrid through the project ADITIMAT-CM (Ref. S2018/NMT-4411) and by the Universidad Carlos III de Madrid (Read & Publish Agreement CRUE-CSIC 2023).

Data availability

No data was used for the research described in the article.

References

[1] P.A. Molian, T.S. Srivatsan, Weldability of aluminium-lithium alloy 2090 using laser welding, J. Mater. Sci. 25 (7) (1990) 3347–3358, https://doi.org/10.1007/BF00587697.
[2] Q.R. Skrabec, Aluminum in America: A History, McFarland, Incorporated, Publishers, Jefferson, North Carolina, 2017.
[3] R.J. Rioja, J. Liu, The evolution of Al-Li base products for aerospace and space applications, Metall. Mater. Trans. A Phys. Metall. Mater. Sci. 43 (9) (2012) 3325–3337.
[4] B.I. Rodgers, P.B. Prangnell, Quantification of the influence of increased pre-stretching on microstructure-strength relationships in the Al–Cu–Li alloy AA2195, Acta Mater. 108 (2016) 55–67, https://doi.org/10.1016/j.actamat.2016.02.017.
[5] N.E. Prasad, Amol Gokhale, R.J.H. Wanhill, Aluminum-lithium Alloys: Processing, Properties, and Applications, Butterworth-Heinemann, 2013.
[6] C. Giummarra, B. Thomas, R. Rioja, New aluminum alloys for aerospace applications, in: Proceedings of the Light Metals Technology Conference, 2007.
[7] N.E. Prasad, T.R. Ramachandran, Phase diagrams and phase reactions in Al–Li alloys, Aluminum-lithium Alloys (Jan. 2014) 61–97, https://doi.org/10.1016/B978-0-12-401698-9.00003-3.
[8] S.C. Wang, M.J. Starink, Precipitates and intermetallic phases in precipitation hardening Al–Cu–Mg–(Li) based alloys, Int. Mater. Rev. 50 (4) (Aug. 2005) 193–215, https://doi.org/10.1179/174328005X14357.
[9] B. Decreus, A. Deschamps, F. De Geuser, P. Donnadieu, C. Sigli, M. Weyland, The influence of Cu/Li ratio on precipitation in Al-Cu-Li-x alloys, Acta Mater. 61 (6) (Apr. 2013) 2207–2218, https://doi.org/10.1016/j.actamat.2012.12.041.
[10] S. Wang, M. Starink, Two types of S phase precipitates in Al-Cu-Mg alloys, Acta Mater. 55 (Feb. 2007) 933–941, https://doi.org/10.1016/j.actamat.2006.09.015.
[11] S. Zhang, Y. Ma, D. Chen, A. Abd, Experimental investigation of tensile properties and anisotropy of 1420, 8090 and 2060 Al-Li alloys sheet undergoing different strain rates and fibre orientation: a comparative study, Procedia Eng. 207 (2017) 13–18, https://doi.org/10.1016/j.proeng.2017.10.730.
[12] A. Abd El-Aty, Y. Xu, X. Guo, S.-H. Zhang, Y. Ma, D. Chen, Strengthening mechanisms, deformation behavior, and anisotropic mechanical properties of Al-Li alloys: a review, J. Adv. Res. 10 (2018) 49–67, https://doi.org/10.1016/j.jare.2017.12.004.
[13] M. Niedzinski, The evolution of constellium Al-Li alloys for space launch and crew module applications, Light Metal Age 77 (1) (2019) 36–42.
[14] S.J. Hales, R.A. Hafley, Aluminum-Lithium alloy thick plate for launch vehicles, in: National Space and Missiles Materials Symposium, 2010.
[15] R.J. Rioja, J. Liu, The evolution of Al-Li base products for aerospace and space applications, Metall. Mater. Trans. A Phys. Metall. Mater. Sci. 43 (9) (2012) 3325–3337.
[16] G. Djukanovic, Aluminium-Lithium alloys fight back. Aluminum Insider: Colmar, France, 2017. https://aluminiuminsider.com/aluminium-lithium-alloys-fight-back/ (accessed Aug. 12, 2022).
[17] P. Rodríguez-González, E.M. Ruiz-Navas, E. Gordo, Effect of heat treatment prior to direct hot-extrusion processing of Al–Cu–Li alloy, Metals (Basel) 12 (6) (Jun. 2022), https://doi.org/10.3390/met12061046.
[18] B. Cai, Z.Q. Zheng, D.Q. He, S.C. Li, H.P. Li, Friction stir weld of 2060 Al-Cu-Li alloy: microstructure and mechanical properties, J. Alloys Compd. 649 (2015) 19–27, https://doi.org/10.1016/j.jallcom.2015.02.124.
[19] X. Jin, B. Fu, C. Zhang, W. Liu, Evolution of the texture and mechanical properties of 2060 alloy during bending, Int. J. Miner. Metall. Mater. 22 (Sep. 2015) 966–971, https://doi.org/10.1007/s12613-015-1156-1.
[20] L.F. Mondolfo, Aluminum Alloys: Structure and Properties, Elsevier Science, 2013.
[21] C. Zubizarreta, S. Gim, J.M. Mart, I. Iturriza, Effect of the heat treatment prior to extrusion on the direct hot-extrusion of aluminium powder compacts 467 (2009) 191–201, https://doi.org/10.1016/j.jallcom.2007.12.035.
[22] B. Cai, Z.Q. Zheng, D.Q. He, S.C. Li, H.P. Li, Friction stir weld of 2060 Al-Cu-Li alloy: microstructure and mechanical properties, J. Alloys Compd. 649 (2015) 19–27, https://doi.org/10.1016/j.jallcom.2015.02.124.
[23] G.B. Schaffer, B.J. Hall, The influence of the atmosphere on the sintering of aluminum, Metall. Mater. Trans. A Phys. Metall. Mater. Sci. (2002), https://doi.org/10.1007/s11661-002-0314-z.
[24] T. Schubert, T. Pieczonka, S. Baunack, B. Kieback, The influence of the atmosphere and impurities on the sintering behaviour of aluminium, Euro PM 2005: Powd. Metall. Congress Exhibit. 1 (September) (2018) 3–8, 2005.
[25] G.B. Schaffer, B.J. Hall, The influence of the atmosphere on the sintering of aluminum, Metall. Mater. Trans. A 33 (10) (2002) 3279–3284.
[26] R.N. Lumley, T.B. Sercombe, G.B. Schaffer, Surface oxide and the role of magnesium during the sintering of aluminum, Metall. Mater. Trans. A Phys. Metall. Mater. Sci. (1999), https://doi.org/10.1007/s11661-999-0335-y.
[27] K. Kondoh, A. Kimura, R. Watanabe, Effect of mg on sintering phenomenon of aluminium alloy powder particle, Powder Metall. (2001), https://doi.org/10.1179/003258901666310.
[28] Y. Ma, X. Liu, Kinetics and thermodynamics of Mg-Al disorder in MgAl2O4-Spinel: a review, Molecules 24 (9) (2019), https://doi.org/10.3390/molecules24091704. MDPI AG.
[29] T. Hiraki, O. Takeda, K. Nakajima, K. Matsubae, S. Nakamura, T. Nagasaka, Thermodynamic criteria for the removal of impurities from end-of-life magnesium alloys by evaporation and flux treatment, Sci. Technol. Adv. Mater. (2011), https://doi.org/10.1088/1468-6996/12/3/035003.
[30] A.V. Dovydenkova, A.I. Klimenko, V.A. Kuznetsov, T.V. Popova, Decomposition of lubricant in compacts from aluminum powder-base mixtures during heating, Soviet Powd. Metall. Metal Ceram. (1981), https://doi.org/10.1007/BF00789196.
[31] C. Li, N. Cheng, Z. Chen, Z. Xie, L. Hui, Intermetallic growth and interfacial properties of the grain refiners in Al alloys, Materials 11 (4) (2018), https://doi.org/10.3390/ma11040636.
[32] J. Augustyn-Pieniążek, H. Adrian, S. Rzadkosz, M. Choroszyński, Structure and mechanical properties of Al-Li alloys as cast, Archiv. Foundry Eng. 13 (2) (2013) 5–10, https://doi.org/10.2478/afe-2013-0027.
[33] J. Zhang, G. Wu, L. Zhang, X. Zhang, C. Shi, J. Sun, Effect of Zn on precipitation evolution and mechanical properties of a high strength cast Al-Li-Cu alloy, Mater. Charact. 160 (Feb. 2020), 110089, https://doi.org/10.1016/J.matchar.2019.110089.
[34] Y. Cao, H. Di, J. Zhang, J. Zhang, T. Ma, R.D.K. Misra, An electron backscattered diffraction study on the dynamic recrystallization behavior of a nickel–chromium alloy (800H) during hot deformation, Mater. Sci. Eng. A 585 (Nov. 2013) 71–85, https://doi.org/10.1016/j.msea.2013.07.037.
[35] V. Vignal, D. Ba, H. Zhang, F. Herbst, S. le Manchet, Influence of the grain orientation spread on the pitting corrosion resistance of duplex stainless steels using electron backscatter diffraction and critical pitting temperature test at the microscale, Corros. Sci. 68 (2013) 275–278, https://doi.org/10.1016/j.corsci.2012.11.013.
[36] S. Zaefferer, P. Romano, F. Friedel, EBSD as a tool to identify and quantify bainite and ferrite in low-alloyed Al-TRIP steels, J. Microsc. 230 (3) (Jun. 2008) 499–508, https://doi.org/10.1111/j.1365-2818.2008.02010.x.
[37] H.H. Bernardi, H.R.Z. Sandim, K.D. Zilnyk, B. Verlinden, D. Raabe, Microstructural stability of a niobium single crystal deformed by equal channel angular pressing, Mater. Res. 20 (5) (Oct. 2017) 1238–1247, https://doi.org/10.1590/1980-5373-MR-2017-0288.
[38] J.K. Mackenzie, Biometrika 45, 1958, p. 229.
[39] J.K. Mackenzie, Acta Metall 12, 1964, p. 223.
[40] J.K. Mackenzie, M.J. Thompson, Biometrika 44, 1957, p. 205.
[41] J. Mason, C. Schuh, The generalized Mackenzie distribution: disorientation angle distributions for arbitrary textures, Acta Mater. 57 (Aug. 2009) 4186–4197, https://doi.org/10.1016/j.actamat.2009.05.016.
[42] V.Yu. Gertsman, A.P. Zhilyaev, A.I. Pshennichnyuk, R.Z. Valiev, Modelling of grain boundary misorientation spectrum in polycrystals with crystallographic texture, Acta Metall. Mater. 40 (6) (1992) 1433–1441, https://doi.org/10.1016/0956-7151(92)90445-K.
[43] H.-G. Brokmeier, Experimental textures of Al-Pb, Al-Cu, and Fe-Cu metal-metal composites, Mater. Sci. Eng. 175 (1994) 131–139.
[44] J. Entringer, M. Reimann, A. Norman, J.F. dos Santos, Influence of Cu/Li ratio on the microstructure evolution of bobbin-tool friction stir welded Al–Cu–Li alloys, J. Mater. Res. Technol. 8 (2) (2019) 2031–2040, https://doi.org/10.1016/j.jmrt.2019.01.014.
[45] Q. Li, X. Zhang, L. Wang, J. Qiao, The effect of extrusion and heat treatment on the microstructure and tensile properties of 2024 aluminum alloy, Materials 15 (21) (Oct. 2022) 7566, https://doi.org/10.3390/ma15217566.
[46] Y. Yang, et al., Effects of hot extrusion and heat treatment on microstructure and properties of industrial large-scale spray-deposited 7055 aluminum alloy, Mater. Res. Express 5 (1) (Jan. 2018) 16519, https://doi.org/10.1088/2053-1591/aaa56b.
[47] K. Bharath, A. Mandal, A. Karmakar, A. Khanra, D.M.J. Davidson, Understanding the effect of hot extrusion on the evolution of microstructure and associated mechanical properties in sintered Al-Cu-Mg alloys, Mater. Charact. 170 (Oct. 2020), https://doi.org/10.1016/j.matchar.2020.110715.
[48] C. Yu, et al., Effect of pre-stretching deformation treatment process on microstructure and mechanical properties of Al-Cu-Mg alloy, Mater Today Commun. 31 (2022), 103368, https://doi.org/10.1016/j.mtcomm.2022.103368.
[49] G.A. Pantazopoulos, A short review on fracture mechanisms of mechanical components operated under industrial process conditions: fractographic analysis and selected prevention strategies, Metals (Basel) 9 (2) (2019), https://doi.org/10.3390/met9020148.